

# An Investigation of the Loss of Planet-Forming Potential in Intermediate Sized Young Embedded Star Clusters

Lisa Holden, Edward Landis, and Jeremy Spitzig

*Department of Mathematics and Statistics, Northern Kentucky University, Highland Heights, KY 41099*

and

Fred C. Adams

*Department of Physics, University of Michigan, Ann Arbor, MI 48109*

## ABSTRACT

A large fraction of stars forming in our galaxy are born within clusters embedded in giant molecular clouds. In these environments, the background UV radiation fields impinging upon circumstellar disks can often dominate over the radiation fields produced by each disk's central star. As a result, this background radiation can drive the evaporation of circumstellar disks and lead to the loss of planet forming potential within a cluster. This paper presents a detailed analysis of this process for clusters whose stellar membership falls within the range  $100 \leq N \leq 1000$ . For these intermediate-sized clusters, the background UV field is often dominated by the most massive stellar member. Due to the steep slope of the initial mass function, the amount of background UV light that bathes clusters of similar size displays significant variance. As a result, we perform a statistical analysis of this problem by calculating distributions of FUV flux values impinging upon star/disk systems for several cluster scenarios. We find that in the absence of dust attenuation, giant planet formation would likely be inhibited in approximately half of systems forming within intermediate-sized clusters regardless of stellar membership. In contrast, the presence of dust can significantly lower this value, with the effect considerably more pronounced in more populated clusters.

*Subject headings:* open clusters and associations: general — planetary systems: formation — stars: formation

## 1. Introduction

The formation of stars within the Milky Way is presently occurring within massive complexes of molecular gas and dust known as giant molecular clouds (GMCs). These highly non-uniform structures typically contain several dense clumps with characteristic densities  $n \sim 10^3 \text{ cm}^{-3}$  and radii in the range  $R = 0.2 - 2 \text{ pc}$ . The largest of these clumps contain as many as  $\sim 1000$  small ( $R \sim 0.1 - 0.2 \text{ pc}$ ), dense ( $\sim 10^4 - 10^5 \text{ cm}^{-3}$ ) condensations called cores, which are the sites of individual star formation events. The mass function of these cores has been measured to span the mass range  $\sim 1 - 100M_{\odot}$  with a peak  $\sim 10M_{\odot}$  (Jijina et al. 1999), and, more recently, a mass range  $\sim 0.2 - 20M_{\odot}$  and a characteristic mass of  $\sim 2M_{\odot}$  (Lada et al. 2008). On the theoretical front, competing paradigms have been developed over the past two decades to explain how the dense regions of GMCs become gravitationally unstable (e.g., Shu et al. 1987; Myers 1998; Klessen & Burkett 2000, 2001; McKee & Ostriker 2007), and subsequently, how the ensuing collapse forms a protostar/disk system (e.g., Shu 1977; Fatuzzo et al. 2004).

Although many of the details describing how stars form remain under study, it is clear that the end result of this complex process is the formation of stellar nurseries containing tens to thousands of members (e.g., Lada & Lada 2003; Porras et al. 2003). Indeed, young embedded clusters appear to be basic units of star formation (e.g., Gutermuth et al. 2009), and they account for perhaps 90% of the stars that populate the Galactic disk. A significant body of work now exists on how these young clusters evolve and how their environment affects the formation processes occurring within. Not surprisingly, early work focused on either small ( $N \leq 100$ ) clusters (e.g., Lada et al. 1984) or large ( $N \geq 10,000$ ) clusters (e.g., Portegies Zwart et al. 1998; Störzer & Hollenbach 1999; Boily & Kroupa 2003). However, about 60% of stars observed in nearby ( $\lesssim 2 \text{ kpc}$ ) embedded clusters belong to intermediate-sized systems with  $N = 100 - 1000$  (Lada & Lada 2003; Porras et al. 2003; see also Adams & Myers 2001).

Motivated by these observational results, Adams et al. (2006) performed a suite of  $N$ -body simulations to explore how the evolution of intermediate sized clusters depends on the system size  $N$  and on initial conditions. One aspect of this previous work was an analysis of how the background FUV fields in embedded clusters affect planetary formation. Toward that end, these authors calculated a probability distribution for the FUV flux experienced by the ensemble of cluster stars in the Lada & Lada (2003) catalog as a function of the FUV flux. Specifically, for each star within a cluster of size  $N$ , a Salpeter IMF was sampled  $N$  times to determine a corresponding cluster background FUV luminosity, where the models of Maeder & Meynet (1987) and Schaller et al. (1992) were used to specify the FUV luminosity as a function of stellar mass. A stellar density profile of the form  $\rho_* \propto r^{-1}$  for  $0 \leq r \leq R_c$  was

then sampled to calculate an effective flux exposure, where the cluster size  $R_c$  was based on a fit to the data obtained by Lada & Lada (2003) and Carpenter (2000). This process was then repeated for all clusters within the catalog in order to ascertain what fraction of stars have orbit-averaged fluxes exceeding benchmark values for which the effects of photoevaporation on circumstellar disks have been calculated in detail (Adams et al. 2004). It is important to note that the effects of dust attenuation were not included in these calculations. Since a substantial amount of gas and dust can be present in the earliest stages of cluster evolution, these results provide an upper limit to the effects of radiation on planetary formation.

The aforementioned statistical investigation was extended by considering how much radiation a given solar system experiences over the course of its orbit. Specifically, the authors used approximate analytical descriptions of orbits in a Hernquist potential (Hernquist 1990) in order to obtain a simple expression (Adams & Bloch 2005) for the mean flux experienced by a star in a cluster of size  $N$  in terms of the star’s (dimensionless) energy  $\epsilon$  and angular momentum  $q$  (see equation [7] for definitions). This expression was later incorporated in follow-up work on the effects of both EUV and FUV background fields on circumstellar disks and planetary formation (Fatuzzo & Adams 2008; see also Armitage 2000). Specifically, the distributions of orbit-averaged fluxes for both EUV and FUV radiation bands were constructed by sampling the orbital parameters  $\epsilon$  and  $q$ . In addition, these authors also considered the effects of dust attenuation in their analysis, and thereby also provided limits on the orbit-averaged flux impinging on young star/disk systems.

This paper builds upon previous work in three important ways: First, this treatment presents a considerably more detailed analysis of how stellar orbits affect the amount of radiation impinging upon the surrounding protoplanetary disks; this work includes generalized forms for the cluster potentials. Second, the stellar orbits are calculated numerically rather than through the previously adopted analytic approximations, thereby yielding greater accuracy in the desired output measures. [For completeness, we also note that the analytical expression presented in Adams et. al (2006) contained a typo so that the results of Fatuzzo & Adams (2008), which used this expression, correspond to the case of nearly circular orbits.] Finally, several different cluster environment scenarios are considered in detail, thereby allowing us to explore how cluster size  $N$ , mass density profile, star formation efficiency, and dust attenuation affects planetary formation.

The timescales of interest in this paper — for cluster evolution, disk evolution, and planet formation — all lie in the range 1 – 10 Myr. Young embedded clusters typically retain their gaseous component for 3 – 5 Myr (Gutermuth et al. 2009) and remain intact for  $\sim 10$  Myr (Lada & Lada 2003; Porras et al. 2003). The lifetime of circumstellar disks is comparable; more specifically, the fraction of the observed disk population that retains

signatures of nebular gas is a decreasing function of time, with a half-life of about  $\sim 3$  Myr and an e-folding time of  $\sim 5$  Myr (Hernández et al. 2007). On a related note, the time required for typical radiation fields to evaporate the outer portions of circumstellar disks is also measured in Myr (Johnstone et al. 1998; Adams et al. 2004; Ercolano et al. 2009). Finally, the timescale for giant planet formation through the core accretion mechanism (Lissauer & Stevenson 2007) is typically 2 – 7 Myr, while the timescale for planet migration is somewhat shorter at  $\sim 1$  Myr (Papaloizou & Terquem 2006).

Although this paper focuses on the effects of radiation, which leads to mass loss in circumstellar disks, we note that cluster environments provide additional influences on forming solar systems: Dynamical interactions between the solar systems and other cluster members can produce tidal truncation of the disks (Clarke & Pringle 1993; Kobayashi & Ida 2001) and/or disruption of the planetary orbits at later times (Adams et al. 2006; Malmberg & Davies 2009). On a related note, the disks can gain mass through Bondi-Hoyle accretion as they orbit through the cluster (Throop & Bally 2008). In cluster environments, massive stars can also influence solar systems through supernova explosions, which can sculpt disks through interactions with their blast waves (Chevalier 2000; Ouelette et al. 2007) and by enriching the disk material with radioactive material (Cameron & Truran 1977; Williams & Gaidos 2007).

The paper is organized as follows. We review the physical characteristics of intermediate sized clusters in §2, with a focus on cases with  $N = 100, 300,$  and  $1000$ . We then consider the orbits of stars that populate these clusters in §3 for two different static density profiles assumed as representative of the true stellar/gas content of the system. In §4, we compute the orbit-averaged FUV flux over a range of orbital parameters for several cluster profiles, obtaining values for cases with and without dust extinction. A statistical analysis is performed in §5 in order to quantify the expected effect on disk-evaporation in clusters of membership size  $N = 100, 300,$  and  $1000$ . The paper then concludes, in §6, with a summary of results and a discussion of their implications.

## 2. The Stellar Populations of Intermediate Sized Clusters

Embedded cluster environments, and in particular, the radiation fields which bathe them, depend sensitively on the population of their stellar members. We consider here the properties of intermediate sized clusters with membership numbers within the range  $100 \leq N \leq 1000$ . Of course, such a characterization can only be done statistically, as two clusters with the same number of members could have considerably different populations, owing in large part, to the steepness of the initial mass function (IMF). In addition, the

(few) large stars produce the most radiation. As a result, most of the FUV light bathing intermediate-sized clusters originates from the most massive stellar member. Given the steepness of the initial mass function, and hence the rarity of massive stars, there is therefore a large variance in the total FUV luminosities of intermediate-sized clusters.

As a starting point, we begin by considering the distribution of star-forming cluster sizes, defined in terms of stellar membership  $N$ . Recent infrared observations have produced catalogs of embedded clusters out to 1 kpc (Porrás et al. 2003) and 2 kpc (Lada & Lada 2003). Of course, both catalogs are almost certainly not complete, with stellar memberships of larger clusters undercounted due to the inability of fully observing all of the faint, low-mass members. In addition, it is also possible that smaller clusters ( $N \lesssim 100$ ) have been missed altogether. Nevertheless, these catalogs are likely representative of the population of intermediate clusters within the disk of our galaxy. The fraction  $f(N)$  of the total number of stars in the union of these catalogs is shown in Figure 1. As can be seen by the dotted reference lines in this figure, nearly 60% of these stars are born in clusters with  $100 \leq N \leq 1000$ , and are evenly distributed logarithmically in  $N$  within this range (shown by the linear fit to the data within this range as denoted by the solid curve). The characteristic membership size for these intermediate clusters is thus  $N_{ch} \approx 300$ , as illustrated by the dashed reference line in Figure 1.

Young embedded clusters are observed to have radii  $R_c$  ranging between 0.1 – 2 pc, with a clear correlation between  $R_c$  and  $N$ , although significant scatter exists in the data (Carpenter 2000; Lada & Lada 2003). We use here the relation

$$R_c = 1.0 \text{ pc } \sqrt{(N/300)}, \quad (1)$$

which is obtained through a simple fit to the aforementioned data (see Figure 1 of Adams et al. 2006). Given that  $\sim 90\%$  of stars have masses less than  $1M_\odot$ , the total stellar mass of a cluster of size  $N$  is expected to be  $M_* \approx 0.5N M_\odot$ . We assume here that this stellar content is contained within  $R_c$ . Of course, the gas from which these stars are born extends much farther, eventually merging smoothly into the GMC background. This gaseous component is eventually disrupted through the action of stellar winds and outflows, radiative processes, and supernovae (e.g., Whitworth 1979; Matzner & McKee 2000; Gutermuth et al. 2004). Although the details of these processes are not fully understood, observations indicate that clusters older than 5 Myrs are rarely associated with molecular gas, so that gas removal must occur on a timescale of  $\sim 3 - 5$  Myr (Lada & Lada 2003).

For an IMF characterized by a probability function  $dP/dm$ , the expectation value  $\langle L_{FUV}^* \rangle$  of the FUV luminosity *per star* is determined by the integral

$$\langle L_{FUV}^* \rangle = \int_{m_{min}}^{m_{max}} L_{FUV}^*(m) \frac{dP}{dm} dm, \quad (2)$$

where  $L_{FUV}^*(m)$  is the stellar FUV luminosity as a function of mass  $m$  (in units of  $M_\odot$ ). We note that the integral is not sensitive to any reasonable value of minimum mass  $m_{min}$ , because most of the FUV light is produced by the most massive stars, in spite of their smaller numbers. Throughout this work, we adopt a stellar IMF with a Salpeter slope at high masses and an upper cutoff  $m_{max} = 100$ . With this IMF, the integral of equation (2) yields a value of  $\langle L_{FUV}^* \rangle = 1.23 \times 10^{36}$  ergs  $s^{-1}$ . In principle, the value  $N\langle L_{FUV}^* \rangle$  can be used to characterize the “typical” FUV luminosity of a cluster of size  $N$ . However, because of the steepness of the IMF, only a small number of high-mass stars are likely to populate intermediate-sized clusters. As a result, the distributions of the maximum stellar masses and FUV luminosities for a population of clusters of size  $N$  are heavily skewed, so that the “typical” maximum stellar mass and FUV luminosity of a cluster are better represented by the median values of the distributions (which are significantly smaller than the mean values). In addition, the total cluster luminosity  $L_{FUV}^c$  is dominated by the the luminosity  $L_{FUV}^{max}$  of the most massive star.

To illustrate these points, we perform a suite of simulations in order to build up distributions of  $m_{max}$ ,  $L_{FUV}^{max}$  and  $L_{FUV}^c$  for clusters with sizes  $N = 100, 300, \text{ and } 1000$ . Specifically, we sample our adopted IMF  $N$  times in order to get the masses of the  $N$  stars which populate our simulated cluster. We use the results presented in Armitage (2000) to obtain the FUV luminosity of each stellar member, thereby finding the total cluster FUV luminosity. We also find the FUV luminosity of the most massive star in the cluster. This procedure is then repeated 100,000 times to build a distribution of luminosities (normalized by  $\langle L_{FUV}^* \rangle$ ) and maximum stellar mass (in units of  $M_\odot$ ) for each assumed cluster size  $N$ .

The luminosity distributions are shown in Figures 2 – 4 for  $N = 100, 300, \text{ and } 1000$ , respectively, where the unshaded (shaded) portions represent the cluster (most massive star) luminosities. The vertical solid and dashed lines denote the median values of the cluster and of the most massive star luminosities, respectively. In addition, one sees that for  $N \lesssim 300$ , the most massive stars do indeed dominate the FUV luminosity of their cluster. For  $N = 1000$ , the most massive star typically provides about half of the total cluster luminosity. The mean and median values of our obtained distributions are summarized in Table 1. As expected, the median values fall well below the expectation values.

### 3. Orbit Solutions

This work focuses on how the average flux that impinges upon a circumstellar disk depends upon the orbit of its parent star and the cluster environment in which it resides. While encounters with other stellar members can alter a star’s orbit, the resulting effects

for intermediate sized clusters are relatively small (Adams et al. 2006) over the timescales for disk evolution and planet formation (3 – 10 Myr). As a result, one can obtain good approximations for stellar orbits by assuming that the stars move through a smooth and time-independent gravitational potential that includes both the gas and stellar content of the cluster. To model this potential, we consider two density profiles of the form

$$\rho(\xi) = \frac{\rho_0}{\xi(1 + \xi)^c}, \quad (3)$$

where  $\xi = r/r_s$  is a dimensionless radius and  $r_s$  is a length scale that characterizes the width of the density profile (the radial size of the cluster). Here we consider two values for the index:  $c = 3, 4$  (see below). This assumed form describes observed clusters in that the density scales as  $1/\xi$  for small values of  $\xi$  and drops off quickly into the background for large values of  $\xi$ . Note that the radial dependence  $\rho \sim 1/\xi \sim 1/r$  for gas in clusters (and cluster-forming cores) has been inferred from observations (e.g., Larson 1985; Jijina et al. 1999). For simplicity, we set  $r_s = R_c = 1.0 \text{ pc} \sqrt{N/300}$  throughout this paper (consistent with the observations of Lada & Lada [2003] and the scaling law of equation [1]). As shown below, orbit solutions can be obtained in terms of two dimensionless quantities that characterize the energy and angular momentum of the stellar orbit. These orbits can then be placed in a desired cluster environment through the proper choice of the density scale  $\rho_0$ , as carried out in §4.

We characterize the orbit solutions for both the Hernquist potential ( $c = 3$ ) and the steeper modified Hernquist potential ( $c = 4$ ). Both cases yield analytical results and thereby provide a convenient framework from which to explore the orbit solutions. The orbit solutions for the Hernquist potential have been explored in detail (Adams & Bloch 2005). Here we summarize these previous results and extend the analysis to include the modified Hernquist potential. The Hernquist gravitational potential ( $c = 3$ ) and corresponding mass profile are given by the expressions

$$\Psi(\xi) = \frac{\Psi_0}{1 + \xi}, \quad M(\xi) = M_\infty \frac{\xi^2}{(1 + \xi)^2}, \quad (4)$$

where  $\Psi_0 \equiv 2\pi G\rho_0 r_s^2$  is the total depth of the gravitational potential and  $M_\infty \equiv 2\pi r_s^3 \rho_0$  is the total mass. The corresponding expressions for the modified Hernquist gravitational potential ( $c = 4$ ) are

$$\Psi(\xi) = \Psi_0 \frac{(2 + \xi)}{2(1 + \xi)^2}, \quad M(\xi) = M_\infty \frac{\xi^3 + 3\xi^2}{(1 + \xi)^3}, \quad (5)$$

where  $\Psi_0 \equiv 4\pi G\rho_0 r_s^2/3$  and  $M_\infty \equiv 2\pi r_s^3 \rho_0/3$ . Note that all quantities are taken to be positive, with the proper signs inserted as necessary.

### 3.1. General Orbits

Orbits in spherical mass distributions are governed by the following differential equation (Binney & Tremaine 1987)

$$\frac{d\theta}{dr} = \frac{1}{r} \left[ \frac{2(E - V)r^2}{j^2} - 1 \right]^{-1/2}, \quad (6)$$

where  $V$  is the potential,  $E$  is the energy, and  $j$  is the specific angular momentum. We consider only bound orbits with negative energy. Following Adams & Bloch (2005), we introduce the dimensionless variables

$$\epsilon \equiv |E|/\Psi_0, \quad q \equiv j^2/2\Psi_0 r_s^2. \quad (7)$$

Equation (6) can thus be written in dimensionless form as

$$\xi \frac{d\theta}{d\xi} = [q/f(\xi)]^{1/2}, \quad (8)$$

where the rational function  $f(\xi)$  determines the properties of the orbits. For the Hernquist potential, this function takes the form

$$f_H(\xi) = -\epsilon\xi^2 + \frac{\xi^2}{1 + \xi} - q, \quad (9)$$

whereas the modified Hernquist potential yields the form

$$f_M(\xi) = -\epsilon\xi^2 + \frac{\xi^2(2 + \xi)}{2(1 + \xi)^2} - q. \quad (10)$$

Orbits can exist only over radii where the function  $f(\xi)$  is positive. For values of the parameters  $\epsilon$  and  $q$  that correspond to bound orbits, the expression  $f(\xi)$  has two real positive zeroes,  $\xi_1$  and  $\xi_2$ , such that  $f(\xi)$  is positive for  $\xi_1 < \xi < \xi_2$ . The values  $\xi_1$  and  $\xi_2$  correspond to the radial turning points of the orbit, as shown by the spirographic orbit depicted in Figure 5. For a given value of  $c$ , the turning points may need to be found numerically for each set of  $\epsilon$  and  $q$ . However, the inverse relations can be written down explicitly (analytically) and take the forms

$$\epsilon = \frac{\xi_1(1 + \xi_2)^{c-2} - \xi_2(1 + \xi_1)^{c-2} + (\xi_2 - \xi_1)(1 + \xi_2)^{c-2}(1 + \xi_1)^{c-2}}{(\xi_2 - \xi_1)(\xi_1 + \xi_2)(c - 2)(1 + \xi_1)^{c-2}(1 + \xi_2)^{c-2}}, \quad (11)$$

$$q = \xi_1\xi_2 \frac{\xi_1(1 + \xi_1)^{c-2} - \xi_2(1 + \xi_2)^{c-2} + (\xi_2 - \xi_1)(1 + \xi_2)^{c-2}(1 + \xi_1)^{c-2}}{(\xi_2 - \xi_1)(\xi_1 + \xi_2)(c - 2)(1 + \xi_1)^{c-2}(1 + \xi_2)^{c-2}}. \quad (12)$$



For the Hernquist profile ( $c = 3$ ), these expressions reduce to previously known results [see equation (6) from Adams & Bloch (2005)]; for the modified Hernquist potential ( $c = 4$ ) these results are new. Notice also that the term  $(\xi_2 - \xi_1)$  term can be factored out of the numerator, for both expressions and for both  $c = 3$  and 4; these expressions are thus non-singular.

In contrast to orbits in a Keplerian potential, the energy parameter in cluster potentials varies over a finite range, where  $0 < \epsilon < 1$ . The value of  $\epsilon$  determines the radial scale of the orbit, where  $\epsilon = 0$  corresponds to a star that is outside the potential well of the cluster environment ( $r \rightarrow \infty$ ) and  $\epsilon = 1$  corresponds to a star at rest in the cluster center ( $r \rightarrow 0$ ). The angular momentum parameter  $q$  characterizes the effective “eccentricity” of the spirographic orbit, with  $q = 0$  corresponding to a purely radial orbit. For a specific value of the energy parameter  $\epsilon$ , the maximum value of  $q$  for which bound orbits exist occurs where  $\xi_1$  and  $\xi_2$  coincide, and this case thus corresponds to a circular orbit. For the Hernquist potential, the maximum value  $q_{max}$  in terms of  $\epsilon$  can be found analytically by solving equations (11) and (12) with  $\xi_1 = \xi_2$ , yielding the expression

$$q_{max} = \frac{1}{\epsilon} \frac{(1 + \sqrt{1 + 8\epsilon} - 4\epsilon)^3}{(1 + \sqrt{1 + 8\epsilon})^2}. \quad (13)$$

For the modified Hernquist potential, this procedure requires the solution of a cubic polynomial and is most easily performed numerically.

#### 4. Orbit Average Flux Calculations

The FUV flux impinging upon the circumstellar disk surrounding a star belonging to a young cluster can vary greatly over the course of the stellar orbit. Taking into account this effect, we can gauge the efficiency with which the background FUV luminosity can drive the evaporation of circumstellar disks by calculating orbit-averaged FUV flux values for several different cluster profiles, as defined by the four following criteria:

*Cluster membership N.* – As shown in Figure 1, the majority of stars appear to form in clusters with stellar membership  $N$  in the range  $100 \leq N \leq 1000$ . We sample this range by considering three values of cluster membership:  $N = 100, 300$  and  $1000$ . For each choice of  $N$ , the cluster radius is set through the relation given by Equation (1), and the total stellar mass for the cluster is taken to be  $M_* = 0.5NM_\odot$ . For simplicity, we consider only the FUV luminosity produced by the most massive stellar member, which is assumed to reside at the center of the cluster. Given the skewed nature of the distributions of cluster luminosities obtained in §2, we adopt the median values listed in Table 1 for both the luminosity and maximum stellar mass.

*Star formation efficiency.* – Observational determinations of the star formation efficiency in nearby embedded clusters, though uncertain, range between  $\eta = 0.1 - 0.3$  (Lada & Lada 2003). We consider two values – the midpoint value  $\eta = 1/5$  of this range and the value  $\eta = 1/3$  as adopted by Adams et al. (2006). We assume that all stars form within a radius  $R_c$ , so that  $\eta = M_*/M_1$  where  $M_1$  is the *total* mass of the gas and stars contained within the radius  $R_c$ .

*Gas density profile.* – We assume that the gas and stellar contents of a young cluster are suitably described by a smooth mass density profile of the form given in Equation (3) with  $r_s = R_c$ , and consider cases for which  $c = 3$  (Hernquist profile) and  $c = 4$  (modified Hernquist profile). We connect the value of  $\rho_0$  to each scenario through the relations

$$\rho_0 = \frac{2M_1}{\pi r_s^3} \quad (\text{for } c = 3), \quad \text{and} \quad \rho_0 = \frac{3M_1}{\pi r_s^3} \quad (\text{for } c = 4), \quad (14)$$

where  $M_1 = \int_0^{R_c} 4\pi r^2 \rho(r) dr = M_\infty/4$  if  $c = 3$  and  $M_1 = M_\infty/2$  for  $c = 4$ . Expressing  $\rho_0$  in terms of the star formation efficiency and stellar membership, we find that

$$\rho_0 = \frac{300M_\odot}{\pi(1.0 \text{ pc})^3} \eta^{-1} \left( \frac{N}{300} \right)^{-1/2} \quad (\text{for } c = 3), \quad (15)$$

and

$$\rho_0 = \frac{900M_\odot}{2\pi(1.0 \text{ pc})^3} \eta^{-1} \left( \frac{N}{300} \right)^{-1/2} \quad (\text{for } c = 4). \quad (16)$$

*Dust Attenuation.* – We calculate the orbit-averaged flux both with and without dust attenuation. When considering dust attenuation, we assume that a mass  $Qm_{max}$  of gas and dust collapses to form the central star, and consider values of  $Q = 3$  and  $Q = 10$  in our analysis. Since  $Q > 1$ , we are thus assuming that the star formation process in the central region of the cluster is not 100 percent efficient. The radius of the void surrounding the central star is obtained by setting  $Qm_{max}$  equal to  $M(\xi_c)$ , thereby yielding

$$\xi_c = \frac{Qm_{max} + \sqrt{Qm_{max}2\pi\rho_0R_c^3}}{2\pi\rho_0R_c^3 - Qm_{max}} \quad (17)$$

when  $c = 3$ . As with  $q_{max}$ , this quantity is best obtained numerically when  $c = 4$ . We assume a gas density  $\rho_g(\xi) = (1 - \eta)\rho(\xi)$  beyond a radius  $\xi_c$ . The optical depth outside the void is therefore given by the expression

$$\tau_{FUV}(\xi) = N_{col}(\xi) \sigma_{FUV} = R_c \sigma_{FUV} \int_{\xi_c}^{\xi} \frac{\rho_g(\xi')}{m_H} d\xi', \quad (18)$$

where we adopt a value of  $\sigma_{FUV} = 8 \times 10^{-22} \text{ cm}^2$  for the dust cross-section per Hydrogen nucleus (Störzer & Hollenbach 1999). We note that the integral in equation (18) can be solved analytically for both  $c = 3$  and  $c = 4$ .

For convenience, we introduce a dimensionless time  $\tau \equiv t/\tau_0$ , where  $\tau_0 \equiv r_s/\sqrt{2\Psi_0}$ . The (dimensionless) orbital period can be obtained through the expression

$$\tau_{orb} = 2 \int_{\xi_1}^{\xi_2} \frac{\xi}{\sqrt{f(\xi)}} d\xi, \quad (19)$$

and is shown in Figure 6 as a function of dimensionless energy  $\epsilon$  for our three chosen values of  $N$  and the two density profiles (we note that  $\tau_{orbit}$  is not sensitive to  $q$ ). The corresponding values of the orbital period are smaller for the  $c = 4$  case, as expected, given the proportionality  $\tau_0 \propto \rho_0^{-1/2}$ . These results indicate that stars will complete at least one orbit before the gas and dust are removed by the action of stellar winds (which, as noted in §2, occurs on a timescale of 3 – 5 Myr).

In the absence of dust attenuation, the orbit-averaged FUV flux is given by the expression

$$\langle F_{FUV} \rangle = \frac{L_{FUV}^{max}}{4\pi R_c^2} \frac{1}{\tau_{orb}} \int_0^{\tau_{orb}} \frac{d\tau}{\xi^2}, \quad (20)$$

where the orbital radius  $\xi$  of the star as a function of time is obtained by numerical integration of the governing force equations. The effects of dust attenuation are easily included by multiplying the integrand in equation (20) by a factor of  $\exp[-\tau_{FUV}]$ , where  $\tau_{FUV}$  is the optical depth to FUV radiation for a given point along the orbit.

We calculate values of the orbit-averaged flux for a range of energies  $\epsilon$  corresponding to orbits with radii less than  $R_c$  and at three values of  $q/q_{max}$  for 27 cluster profiles (defined through a choice of  $N$ ,  $\eta$ ,  $c$  and dust scenario). A subset of these results are presented in Figures 7 – 9. In each figure, the horizontal dotted line represents our benchmark value for determining whether the planet-forming potential of a circumstellar disk has been compromised by the background FUV radiation. As a working benchmark value, we use the flux  $G_B = 4.8 \text{ ergs s}^{-1} \text{ cm}^{-2} = 3000 G_0$  (where  $G_0 = 1.6 \times 10^{-3} \text{ ergs s}^{-1} \text{ cm}^{-2}$ ); with this radiation level, the disk surrounding a star with mass  $M_* = 1 M_\odot$  would be reduced to a radius of  $\sim 36 \text{ AU}$  over the course of 10 Myr (Adams et al. 2004). Since giant planets form in the 5 – 30 AU region, over a comparable timescale, star/disk systems that experience an average flux greater than  $\sim G_B$  are expected to have a diminished planet-forming potential. The truncation of circumstellar disks exposed to a given level of FUV flux depends on the mass of the central star. For the benchmark flux value  $G_B$ , a star with mass  $M_* = 0.5 (0.25) M_\odot$  will evaporate down to 18 (9) AU over the course of 10 Myr.

The full set of results for all of the sampled cluster environments are qualitatively described by Figures 7 – 9. In addition, we can summarize these results by specifying the value of energy  $\epsilon_b$  for which the orbit-averaged flux equals our benchmark value. These values of  $\epsilon_b$  are listed in Table 2.

## 5. Statistical Analysis for Clusters

As illustrated in Figures 2 – 4, the steep nature of the stellar IMF results in a large variance in the FUV luminosities for intermediate sized clusters with the same number of stars. Subsequently, the efficiency with which circumstellar disks are evaporated by background FUV fields can vary greatly from cluster to cluster. We therefore present a statistical analysis of the amount of FUV radiation impinging upon cluster members. Since one focus of this work is to determine how the cluster membership size  $N$  affects planetary formation, we first adopt values of  $c = 3$  and  $\eta = 1/5$  (as suggested from observations), and calculate the distribution of FUV flux values experienced by stars for clusters of size  $N = 100, 300,$  and  $1000$ . We note that the evaporation of stars would be more pronounced for a higher star formation efficiency and a steeper density profile, as can be seen by comparing values of  $\epsilon_b$  for the various cases presented in Table 2. Flux values are calculated for both the case of no dust attenuation and the case with dust attenuation and mass depletion parameter  $Q = 3$ . These two classes of results thus represent upper limits (no dust) and lower limits (maximum dust) to the average flux experienced by the stars within the specified cluster environment.

The stellar dynamics of a cluster determines the distribution of energy and angular momentum for the stellar members (e.g., Binney & Tremaine 1987). One can therefore find the relationship between the differential energy distribution, and the density profile of the cluster for a given set of assumptions about the velocity distribution. We adopt here an isotropic velocity distribution and a density profile form  $\rho \propto 1/r$ , corresponding to the limit regimes of our chosen density profiles (since we assume that stars are formed within a radius  $R_c$ ). For this case, the differential energy distribution — the probability distribution for orbital energies — takes the form

$$h(\epsilon) = \frac{dP_m}{d\epsilon} = \frac{2}{(1 - \epsilon_0)^2}(1 - \epsilon), \quad (21)$$

which is normalized for the range of dimensionless energies  $\epsilon_0 \leq \epsilon \leq 1$ . Given our assumption that stars are found within  $R_c$ , we truncate the distribution at  $\epsilon_0 = 0.375$ .

The probability distribution for orbital angular momentum depends on the initial velocities with which the stars are born. Recent observations of pre-stellar cores suggest that

these starting velocities are lower than the values expected for virial equilibrium (e.g., André 2002; Peretto et al. 2006). One might therefore expect that stars in clusters have preferentially lower values of  $q/q_{max}$ . However, these lower initial velocities allow the entire cluster to shrink after the stars form and enter into ballistic orbits. In the resulting smaller dynamical system, smaller amounts of angular momentum “go farther” and result in somewhat larger  $q$  values for stellar orbits in the cluster. As a result, stars in nascent clusters tend to have intermediate values of  $q$  (Adams et al. 2006). For simplicity we assume that the probability distribution for orbital angular momentum is uniform (though we consider a particular case with circular orbits below).

For each cluster size, the adopted IMF (see §2) is sampled  $N$  times in order to obtain a value for the most massive star in the cluster, which is assumed to be centrally located. The results presented in Armitage (2000) are then used to obtain a corresponding FUV luminosity (see also Maeder & Meynet 1987; Schaller et al. 1992). Values of  $\epsilon$  and  $q/q_{max}$  are randomly selected from their corresponding probability distributions, and the procedure outlined in §4 is then used to calculate the orbit-averaged flux for the cases of no dust attenuation and dust attenuation with  $Q = 3$ . This process is repeated 10,000 times in order to build up a sample distribution. The results are presented in Figures 10 – 12 for the cases of  $N = 100, 300, \text{ and } 1000$ , respectively, where the unshaded histogram represents the case of no dust attenuation and the shaded histogram represents the case with dust attenuation. The solid vertical line denotes our benchmark value  $G_B = 3000 G_0$ , and the vertical dashed lines denote the median values of the distributions (the lower value corresponding to the case with dust attenuation).

As illustrated by the median values of the calculated distributions, the radial size of a cluster does not significantly affect the amount of FUV flux impinging upon its members in the absence of dust attenuation (this result follows from the assumed/observed scaling law of equation [1] for cluster radii). To quantify this point further, we note that 37%, 53%, and 63% of the stars in the populations shown by the unshaded histograms (no dust) in Figures 10, 11 and 12, respectively, experienced FUV flux values greater than our benchmark value. In contrast, the presence of dust can significantly reduce the FUV flux impinging upon cluster members, with larger clusters better able to shield stellar systems from the central FUV radiation. Interestingly, however, 30%, 33%, and 27% of the stars in the populations shown by the shaded histograms (dust) in Figures 10, 11 and 12, respectively, experienced FUV flux values greater than our benchmark value. Thus, although stars are better shielded from the FUV radiation in larger clusters on the whole, the efficiency with which the formation of giant planets is inhibited (in the presence of dust attenuation) is nearly the same in all medium-sized clusters. This universality results from the fact that while larger clusters have greater column densities, the net effect of dust attenuation is offset by the larger central void

regions associated with more massive stars. As such, stars in smaller clusters are as likely to enter the central void as their counterparts in larger clusters. Indeed, the high-flux peaks of the distributions shown in Figures 10 – 12 for the case of dust attenuation represent the stars that enter this void.

The results presented in §4 suggest that disk photoevaporation is more efficient for clusters with steeper density profiles. This trend occurs because clusters with steeper density profiles have a greater concentration of mass at their centers; as a result, orbits with a given energy  $\epsilon$  will be tighter, leading to an increase in radiative flux. To illustrate this point further, we calculate the distribution of FUV flux values experienced by stars for a cluster of size  $N = 300$  and a star formation efficiency of  $\eta = 1/5$  (as with the case presented in Figure 11), but with a steeper  $c = 4$  density profile. The result is presented in Figure 13. Comparing with Figure 11, we find that the median flux values — both for the case of no dust and dust attenuation — are greater for the  $c = 4$  case. Indeed, 68% of the stars in the population shown by the unshaded histogram (no dust) in Figure 13 experienced FUV flux values greater than our benchmark value (compared with only 53% when  $c = 3$ ), and 45% of the stars in the population shown by the shaded histogram (dust) experienced flux values greater than the benchmark value (compared with 33% when  $c = 3$ ).

As a final point of analysis, we consider what role our assumed distribution of  $q$  values (which determine orbital angular momentum) has on the results presented above. Toward that end, we recalculate the flux distribution shown in Figure 11, but use purely circular orbits (i.e., we set  $q = q_{max}$ ). The resulting flux distributions are shown in Figure 14. Not surprisingly, this change has relatively little effect on the flux experienced by stellar members for the case with no dust, where 46% of stars experience flux values greater than the benchmark value (compared with 53% found in Figure 11). However, adopting circular orbits means that stars born outside of the central void will always remain outside. As a result, the median of the distribution representing the case including dust attenuation is significantly lower for the population shown in Figure 14 than for that shown in Figure 11. In Figure 14, only about 15% of the stars in the population shown by the shaded histogram (with dust) experience FUV flux values greater than our benchmark value, or about half of the corresponding value shown in Figure 11.

## 6. Conclusion

This paper explores the effects of background FUV radiation fields on the planet forming potential of young stars within intermediate-sized clusters. Our results are summarized as follows:

We have determined the distributions of FUV flux levels in young clusters, including the effects of stellar orbits. The orbits of stars in clusters can be described in terms of two dimensionless orbital parameters, the dimensionless energy  $\epsilon$  and angular momentum  $q$ . A star’s orbital period depends primarily on the energy and is longer for larger clusters. Despite a large range in their periods, almost all stars born in intermediate sized clusters complete at least one orbit before stellar outflows, radiation, and supernovae remove the surrounding gas and dust (which is expected to take  $\sim 3 - 5$  Myrs), and typically execute several orbits before planets form within their circumstellar disks ( $\sim 10$  Myr). As a result, orbit-averaged flux values provide useful measures from which to gauge how efficiently the cluster background FUV radiation evaporates disks, and thereby limits planet formation. In this paper, we have constructed distributions of the FUV flux levels that are expected in young embedded clusters (see Figures 10 – 14). These distributions are calculated both with and without the effects of dust attenuation, where the former provides a lower bound and the latter provides an upper bound to the expected radiation levels.

This paper also calculates the values of the orbit-averaged FUV flux impinging upon star/disk systems as a function of orbital energy  $\epsilon$  (see Figures 7 – 9). These calculations are carried out for three values of orbital angular momentum  $q/q_{max}$  and for 27 cluster profiles, defined through a choice of stellar membership  $N$ , star formation efficiency  $\eta$ , density profile index  $c$ , and an assumed dust scenario. Although a full description of cluster radiation fields requires the full distribution of fluxes as shown in Figures 10 – 14, we can summarize the results by presenting the values of dimensionless energy  $\epsilon = \epsilon_b$  for which the orbit-averaged flux equals our adopted benchmark value  $G_B = 3000 G_0$  (see Table 2). [Note that this value of flux causes disks associated with one solar mass stars to experience disruption in giant planet formation.] In general, the orbit-averaged flux experienced by a star/disk system in a given cluster environment increases with the orbital energy  $\epsilon$  and decreases with the orbital angular momentum  $q/q_{max}$ . For similar orbital parameters, stars experience higher flux values when in more populated clusters, clusters with steeper density profiles, and in clusters with greater star formation efficiencies.

Given the steep nature of the IMF, and the relatively modest membership sizes  $N$  considered herein, the efficiency with which circumstellar disks are evaporated by background FUV fields varies greatly from cluster to cluster. Descriptions of FUV radiation fields must thus be represented in a statistical manner. Here we calculate the probability distribution of the orbit-averaged flux for five cluster profiles, both with and without dust attenuation. These results indicate that, in the absence of dust attenuation, between 1/3 and 2/3 of stars in intermediate-sized clusters experience FUV flux values capable of inhibiting giant planet formation, where this fraction increases as the cluster size increases from  $N = 100$  to 1000. Interestingly, although larger clusters are better able to shield stellar systems via

dust attenuation of the central FUV radiation, roughly the same percentage of stars enter the central void associated with the most massive star in the system. As a result, roughly 1/3 of stars will experience FUV flux values greater than our benchmark value regardless of cluster size.

To summarize, this study shows that a substantial fraction (1/3 to 1/2, depending on dust attenuation) of the solar systems born within young embedded clusters are exposed to FUV radiation fields more intense than the benchmark value  $G_B = 3000 G_0 = 4.8 \text{ erg sec}^{-1} \text{ cm}^{-2}$ . By driving photoevaporation, radiation at this level will truncate circumstellar disks surrounding solar type stars to radii  $r \sim 36 \text{ AU}$  over 10 Myr; this timescale is comparable to embedded cluster lifetimes, disk lifetimes, and the time required for giant planets to form. The disks around smaller stars, which are more common, are more easily evaporated. As a result, a large fraction of solar systems are affected by the background radiation in their birth clusters. However, the effects are relatively modest: Although the outer parts of the disks can be truncated, regions near  $r \sim 5 \text{ AU}$ , where planets are most easily formed, are generally left unscathed. As a result, these radiative effects are neither negligible nor dominant. In addition, the FUV radiation fields produced within young clusters is characterized by a wide distribution, so that assessments of radiative effects must be made statistically.

An important challenge for the future is to compare the theoretical predictions of this work with observations. Since photoevaporation acts to disperse circumstellar material, disk lifetimes should vary with cluster environment. As outlined above, however, one expects a wide range of radiative fluxes — and hence evaporation rates and disk lifetimes — within the same cluster. One must thus compare the full distribution of disk lifetimes for a given cluster with the corresponding distributions in other clusters. This comparison requires a great deal of data, which should be forthcoming in the next decade. In addition to disk lifetimes, one can also use planets as a diagnostic: A number of stars in the solar neighborhood are reported to have planetary companions that can be directly imaged, including HR8799 (Marois et al. 2008), Formalhaut (Kalas et al. 2008), and Beta Pic (Lagrange et al. 2009). These imaged planets reside (and presumably formed) in the outer parts of their solar systems, where circumstellar disks are most easily evaporated. With expected improvements in observational capability, future searches for planetary objects at wide separations (where they can be imaged) will be carried out. The results of this paper suggest that the success rate of these searches will be a function of the star formation environment: Intense UV radiation fields should lead to a suppression of observed planets with large semimajor axes (roughly  $a > 40 \text{ AU}$ ).

We are grateful to Marco Fatuzzo for many useful discussions. Lisa Holden, Edward Landis and Jeremy Spitzig were supported at NKU through a 2009 CINSAM Research Grant.



Edward Landis was also supported through a grant from the Kentucky Space Grant Consortium (grant 4000517KSGC). FCA is supported by the University of Michigan through the Michigan Center for Theoretical Physics, by NASA through the Origins of Solar Systems Program (grant NNX07AP17G), by NSF through the Division of Applied Mathematics (grant DMS-0806756), and by the Foundational Questions Institute (grant RFP1-06-1).

## REFERENCES

- Adams, F. C., & Myers, P. C. 2001, *ApJ*, 553, 744
- Adams, F. C., & Bloch, A. M. 2005, *ApJ*, 629, 204
- Adams, F. C., Hollenbach, D., Laughlin, G., & Gorti, U. 2004, *ApJ*, 611, 360
- Adams, F. C., Proszkow, E. M., Fatuzzo, M. & Myers, P. C. 2006, *ApJ*, 641, 504
- Armitage, P. J. 2000, *A&A*, 362, 968
- Boily, C. M., & Kroupa, P. 2003, *MNRAS*, 338, 665
- Cameron, A.G.W., & Truran, J. W. 1997, *Icarus*, 30, 447
- Carpenter, J. M. 2000, *AJ*, 120, 3139
- Chevalier, R. A. 2000, *ApJ*, 538, L151
- Clarke, C. J., & Pringle, J. E. 1993, *MNRAS*, 261, 190
- Ercolano, B., Clarke, C. J., & Drake, J. J. 2009, *ApJ*, 699, 1639
- Fatuzzo, M., Adams, F. C., & Myers, P. C. 2004, *ApJ*, 615, 813
- Fatuzzo, M., & Adams, F. C. 2008, *ApJ*, 675, 1361
- Gutermuth, R. A., Megeath, S. T., Myers, P. C., Allen, L. E., Pipher, J. L., & Fazio, G. G. 2009, *ApJS*, 184, 18
- Hernquist, L. 1990, *ApJ*, 356, 359
- Jijina, J., Myers, P. C., & Adams, F. C. 1999, *ApJS*, 125, 161
- Johnstone, D., Hollenbach, D., & Bally, J. 1998, *ApJ*, 499, 758
- Hernández, J. et al. 2007, *ApJ*, 662, 1067

- Kalas, P., Graham, J. R., Chiang, E., Fitzgerald, M. P., Clampin, M., Kite, E. S., Stapelfeldt, K., Marois, C., & Krist, J. 2008, *Science*, 322, 1345
- Klessen, R. S., & Burkett, A. 2000, *ApJS*, 128, 287
- Klessen, R. S., & Burkett, A. 2000, *ApJ*, 549, 386
- Kobyashi, H., & Ida, S. 2001, *Icarus*, 153, 416
- Lagrange, A. M., et al. 2009, *A&A*, 493, 21
- Lada, C. J., Margulis, M., & Dearborn, D. 1984, *ApJ*, 285, 141
- Lada, C. J., & Lada, E. A. 2003, *ARA&A*, 41, 57
- Lada, C. J., Muench, A. A., Rathborne, J., Alves, J. F., & Lombardi, M. 2008, *ApJ*, 672, 410
- Lissauer, J. J., & Stevenson, D. J. 2007, in *Protostars and Planets V*, ed. B Reipurth, D Jewitt, K Keil, pp. 591–606, (Tucson: Univ. Arizona Press)
- Maeder, A., & Meynet, G. 1987, *A&A*, 182, 243
- Malmberg, D., & Davies, M. B. 2009, *MNRAS*, 394, L26
- Marois, C., Macintosh, B., Barman, T., Zuckerman, B., Song, I., Patience, J., Lafreniere, D., & Doyon, R. 2008, *Science*, 322, 1348
- McKee, C. F., & Ostriker, E. C. 2007, *ARA&A*, 45, 565
- Myers, P. C. 1998, *ApJ*, 496, L109
- Ouelette, N., Desch, S. J., & Hester, J. J. 2007, *ApJ*, 662, 1268
- Papaloizou, J.C.B., & Terquem, C. 2006, *Rep. Prog. Phys.*, 69, 119
- Porras, A., Christopher, M., Allen, L., Di Francesco, J., Megeath, S. T., & Myers, P. C. 2003, *AJ*, 126, 1916
- Portegies Zwart, S. F., Hut, P., Makino, J., & McMillan, S. L. W. 1998, *A&A*, 337, 363
- Schaller, G., Schaerer, D., Meynet, G., & Maeder, A. 1992, *A&AS*, 96, 269
- Shu, F. H. 1977, *ApJ*, 214, 488
- Shu, F. H., Adams, F. C., & Lizano, S. 1987, *ARA&A*, 25, 23

Störzer, H., & Hollenbach, D. 1999, ApJ, 515, 669

Throop, H. B., & Bally, J. 2008, AJ, 135, 2380

Williams, J. P., & Gaidos, E. 2007 ApJ, 663, L33

Table 1. Results from Cluster Simulations

N	Mean Values			Median Values		
	$m_{max}$	$L_{FUV}^{max}/\langle L_{FUV}^* \rangle$	$L_{FUV}^c/\langle L_{FUV}^* \rangle$	$m_{max}$	$L_{FUV}^{max}/\langle L_{FUV}^* \rangle$	$L_{FUV}^c/\langle L_{FUV}^* \rangle$
100	13	90	100	8.1	6.4	8.3
300	24	230	300	17	72	110
1000	42	540	1000	36	390	760

Table 2. Results from Orbit Averaged Flux Calculations

Cluster Parameters				$\epsilon_b$ vs. $q/q_{max}$		
$N$	$\eta$	$c$	$Q$	0.2	0.5	0.8
100	1/3	3	no dust	0.68	0.73	0.75
100	1/3	3	10	0.68	0.73	0.75
100	1/3	3	3	0.70	0.74	0.75
100	1/3	4	no dust	0.58	0.63	0.66
100	1/3	4	10	0.58	0.63	0.66
100	1/3	4	3	0.60	0.66	0.68
100	1/5	3	no dust	0.68	0.73	0.75
100	1/5	3	10	0.69	0.73	0.75
100	1/5	3	3	0.71	0.76	0.78
300	1/3	3	no dust	0.52	0.58	0.60
300	1/3	3	10	0.55	0.60	0.62
300	1/3	3	3	0.58	0.66	0.70
300	1/3	4	no dust	0.40	0.46	0.48
300	1/3	4	10	0.43	0.49	0.51
300	1/3	4	3	0.48	0.57	0.63
300	1/5	3	no dust	0.52	0.58	0.60
300	1/5	3	10	0.56	0.63	0.66
300	1/5	3	3	0.61	0.70	0.76
1000	1/3	3	no dust	0.46	0.51	0.54
1000	1/3	3	10	0.51	0.58	0.61
1000	1/3	3	3	0.57	0.67	0.74
1000	1/3	4	no dust	0.33	0.39	0.41
1000	1/3	4	10	0.39	0.47	0.53
1000	1/3	4	3	0.47	0.60	0.68
1000	1/5	3	no dust	0.46	0.51	0.54
1000	1/5	3	10	0.53	0.62	0.67
1000	1/5	3	3	0.61	0.73	0.79



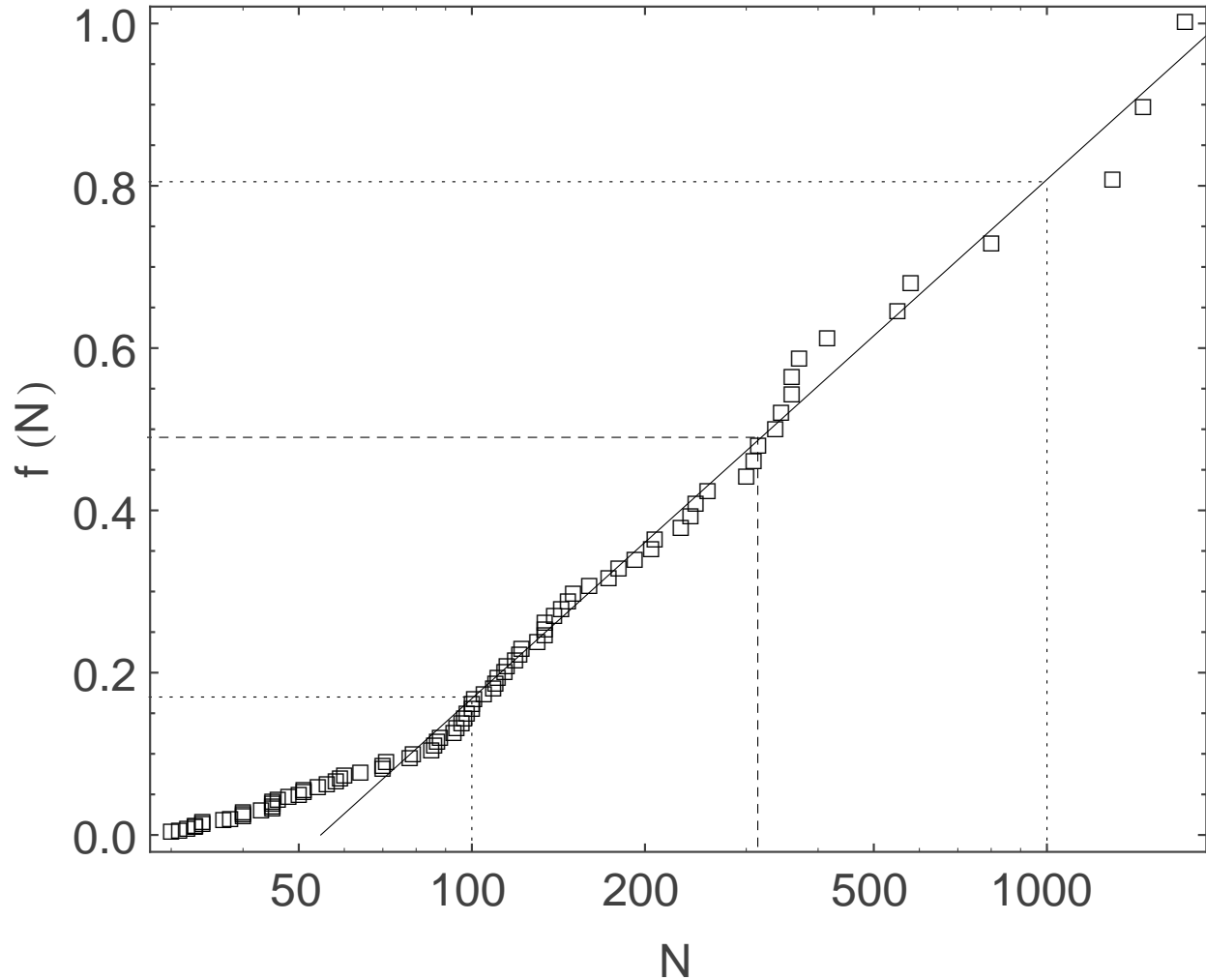


Fig. 1.— Cumulative distribution showing the fraction of stars born in clusters of stellar membership  $N$  as a function of  $N$ . The data points show the combined observed distribution as compiled in Lada & Lada (2003) and Porras et al. (2003). The solid line serves as a reference to illustrate that the number of stars born in clusters of size  $N$  is evenly distributed logarithmically for intermediate sized clusters. The dotted and dashed lines mark the references values discussed in the text.

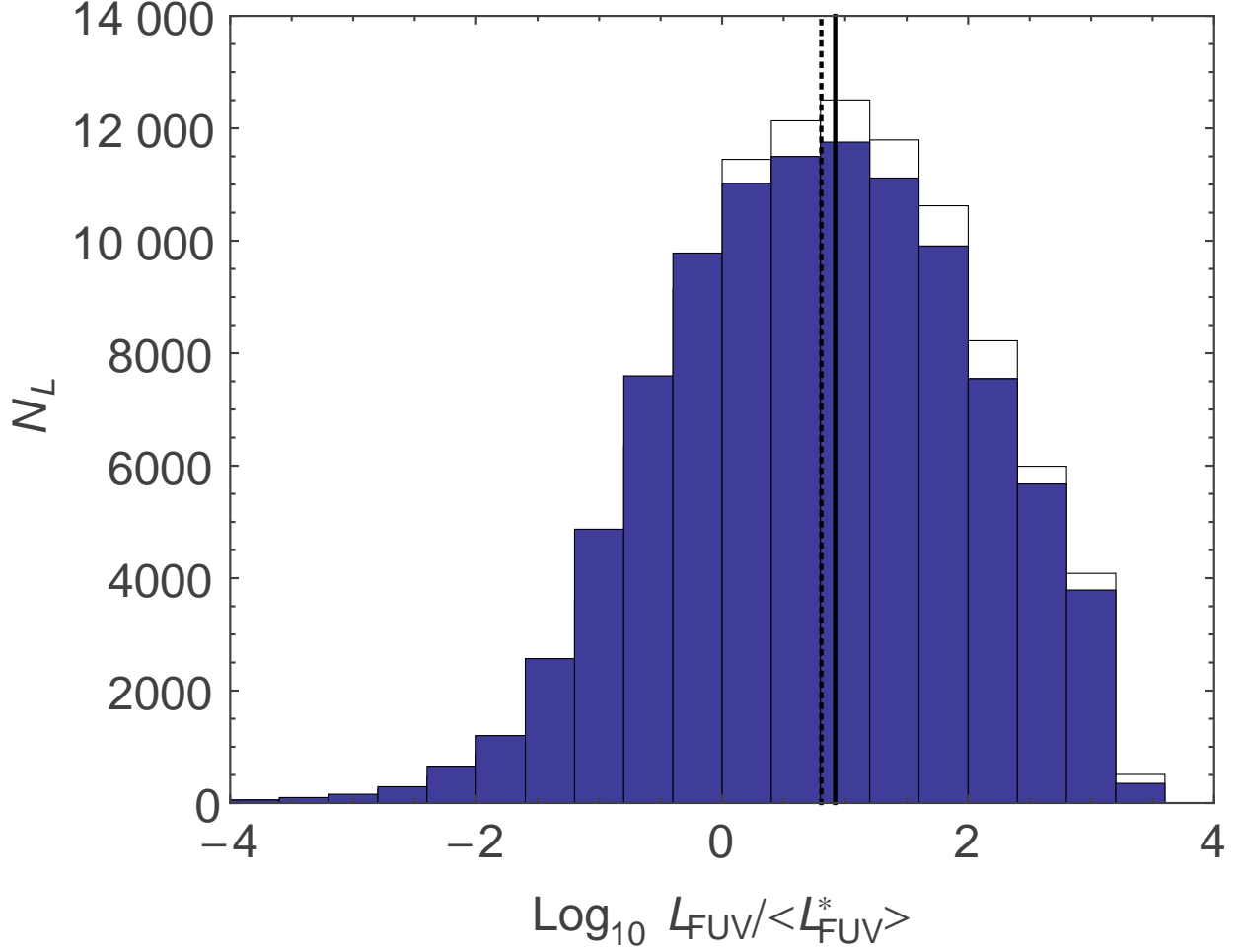


Fig. 2.— Histogram of  $\text{Log}_{10} [L_{FUV}^{max} / \langle L_{FUV}^* \rangle]$  (shaded) and  $\text{Log}_{10} [L_{FUV}^c / \langle L_{FUV}^* \rangle]$  (unshaded) for  $N = 100$ . The distribution was obtained by running 100,000 simulations in which we sample the IMF 100 times to specify the masses and luminosities of the 100 stars that populate each theoretical cluster. The vertical solid and dashed lines denote the median values of luminosity for the cluster and for the most massive star, respectively. We note that the mean value of  $L_{FUV}^{max} / \langle L_{FUV}^* \rangle$  is 90 and the mean value of  $L_{FUV}^c / \langle L_{FUV}^* \rangle$  is 100.



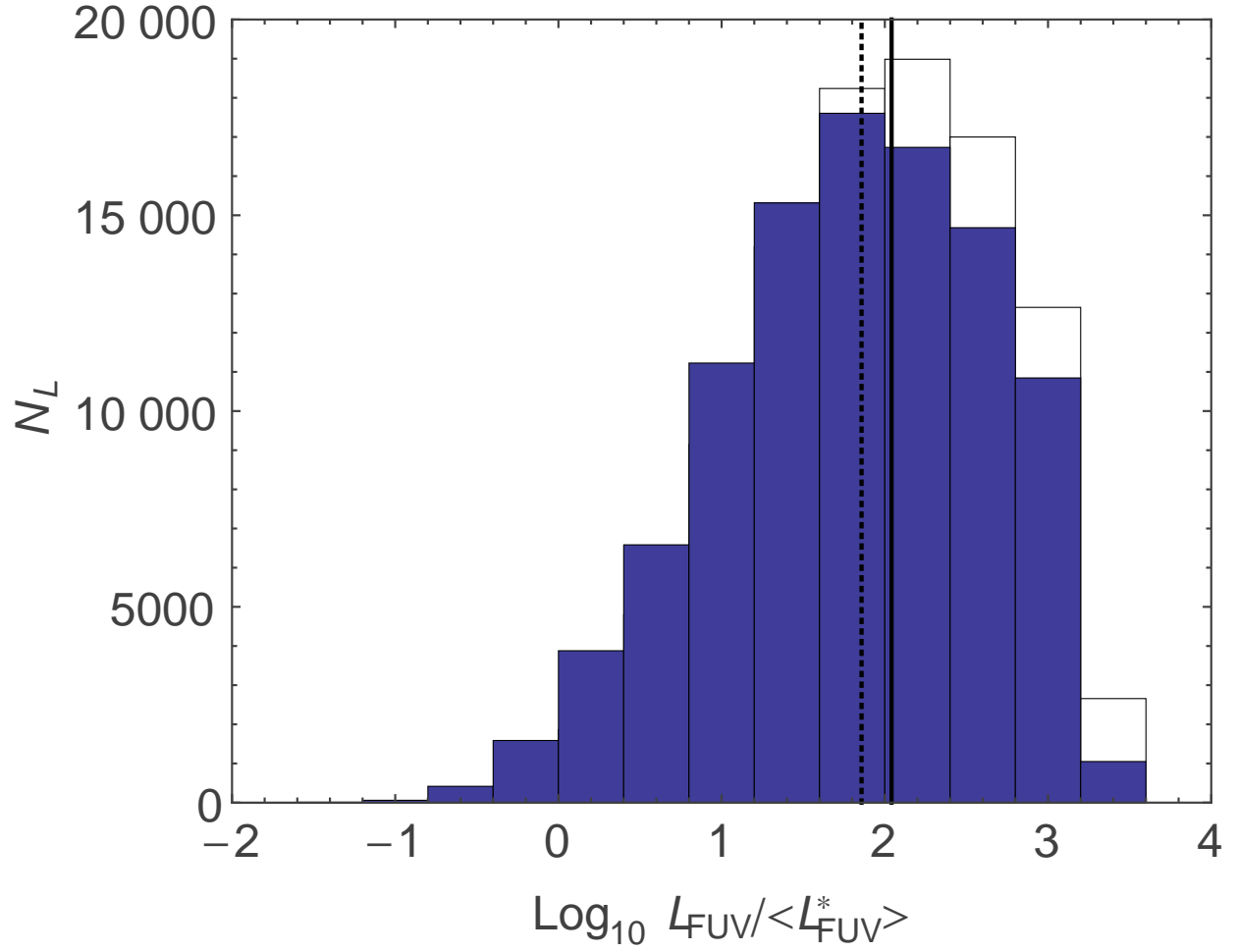


Fig. 3.— Same as Figure 2, but with  $N = 300$ . We note that the mean value of  $L_{FUV}^{max} / \langle L_{FUV}^* \rangle$  is 230 and the mean value of  $L_{FUV}^c / \langle L_{FUV}^* \rangle$  is 300.

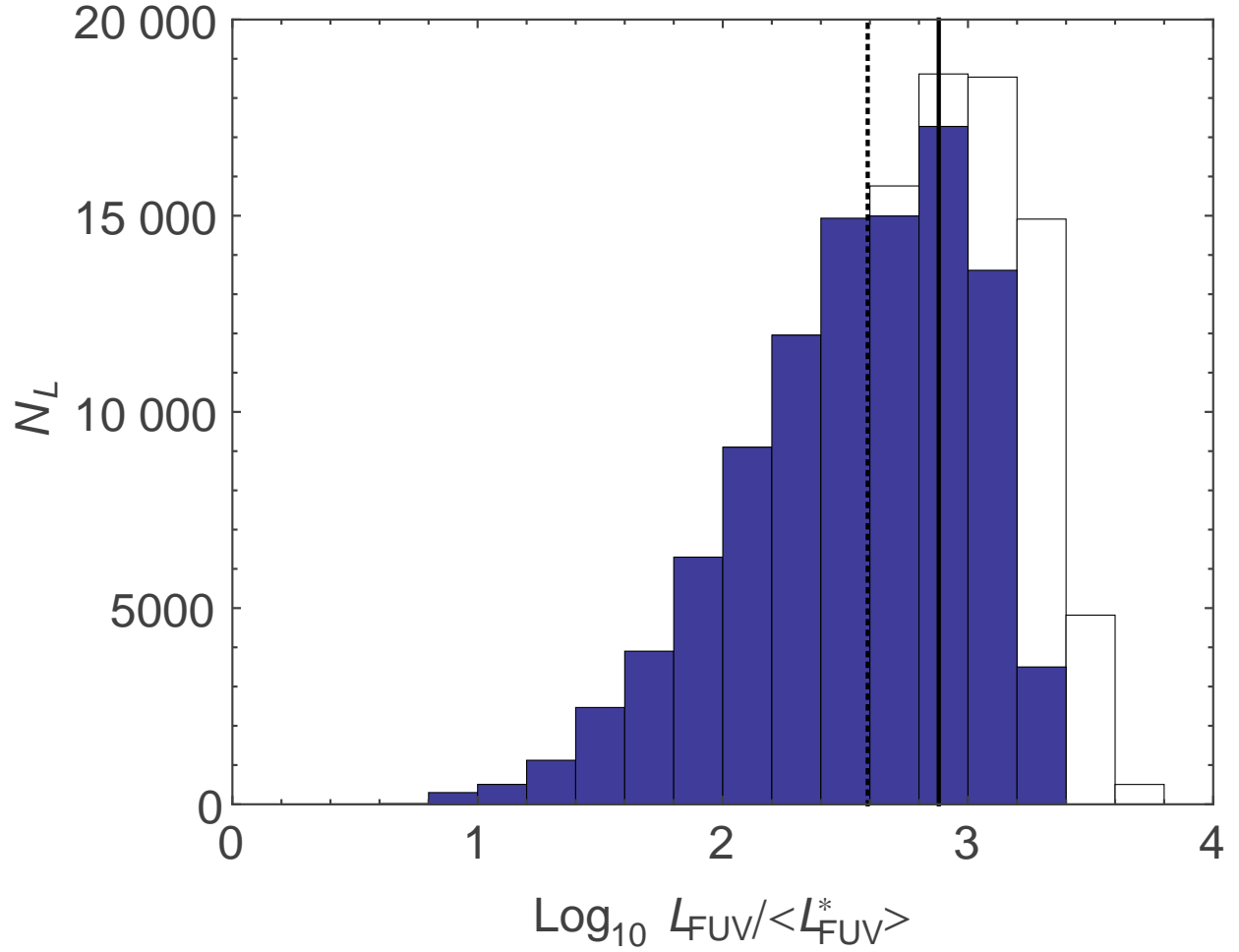


Fig. 4.— Same as Figure 2, but with  $N = 1000$ . We note that the mean value of  $L_{FUV}^{max} / \langle L_{FUV}^* \rangle$  is 540 and the mean value of  $L_{FUV}^c / \langle L_{FUV}^* \rangle$  is 1000.

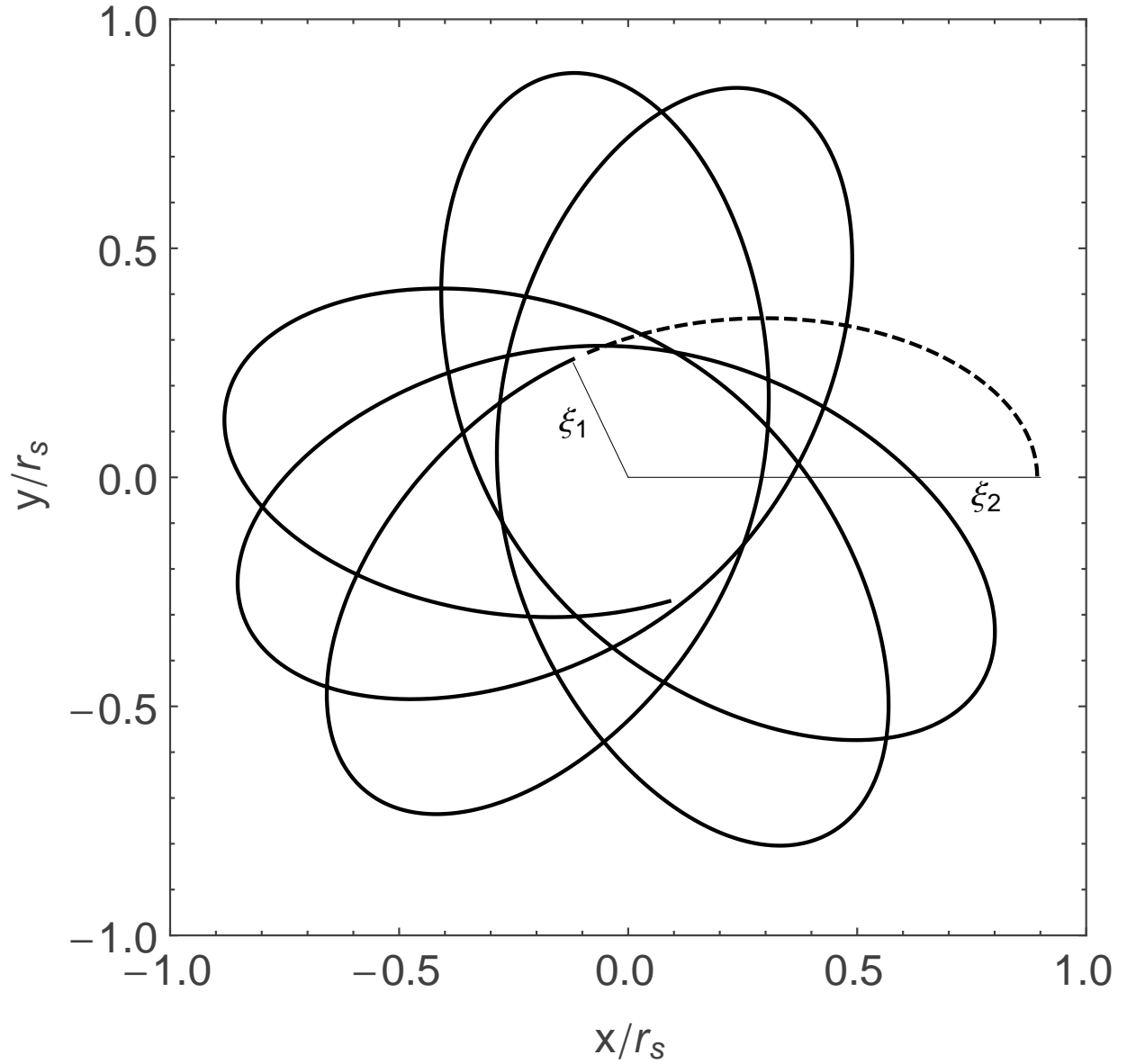


Fig. 5.— Spirographic orbit for dimensionless energy  $\epsilon = 0.5$ , angular momentum variable  $q/q_{max} = 0.5$ , stellar membership  $N = 100$ , and density profile index  $c = 3$  (see text). The dashed curve depicts a half-orbit with the turning points  $\xi_1 = 0.28$  and  $\xi_2 = 0.89$ .

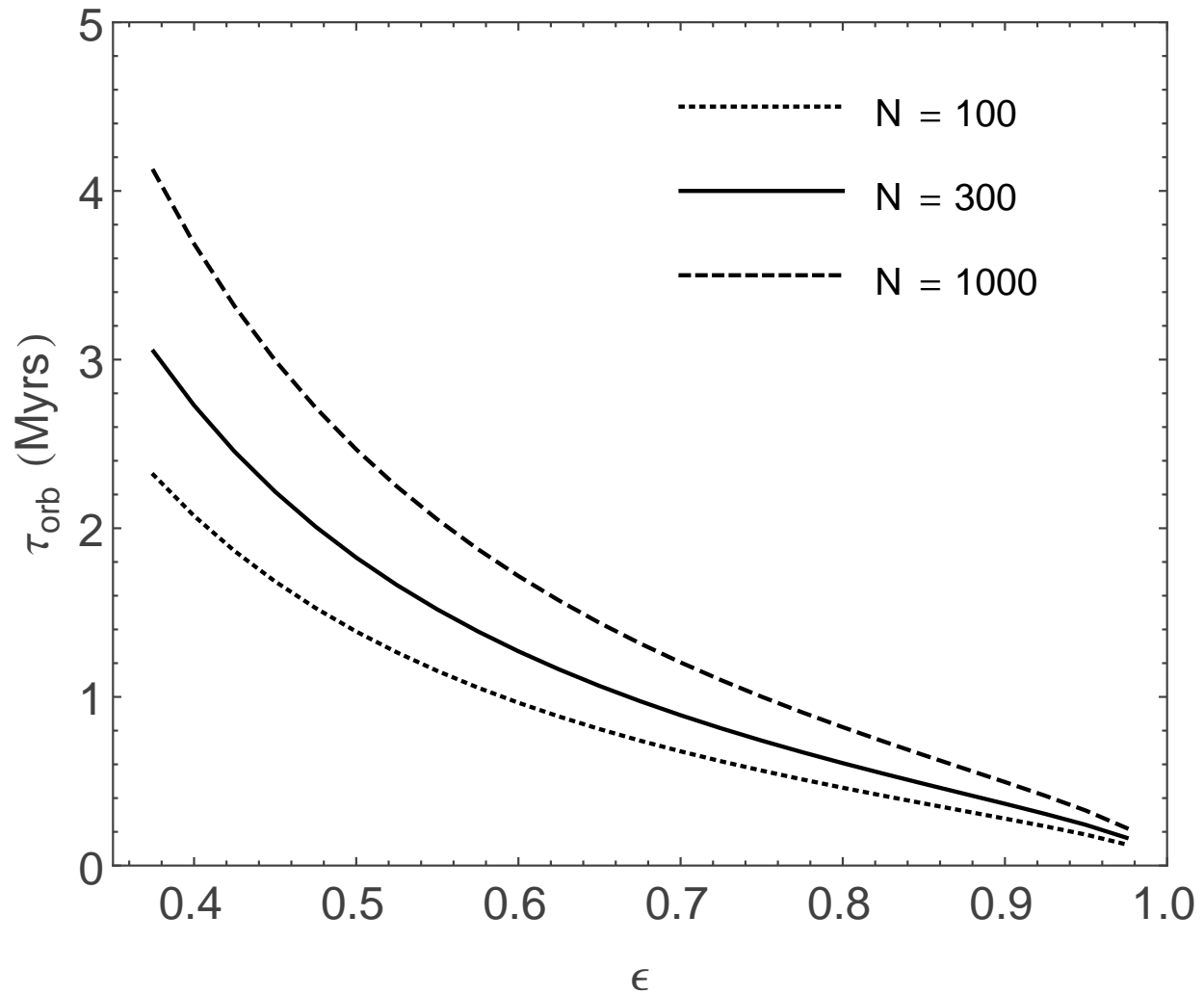


Fig. 6.— Orbital period as a function of dimensionless energy  $\epsilon$  for stars in clusters with membership  $N = 100$  (dotted curve), 300 (solid curve), and 1000 (dashed curve). For each case, the clusters have Hernquist density profiles ( $c = 3$ ) and star formation efficiencies  $\eta = 1/3$ .

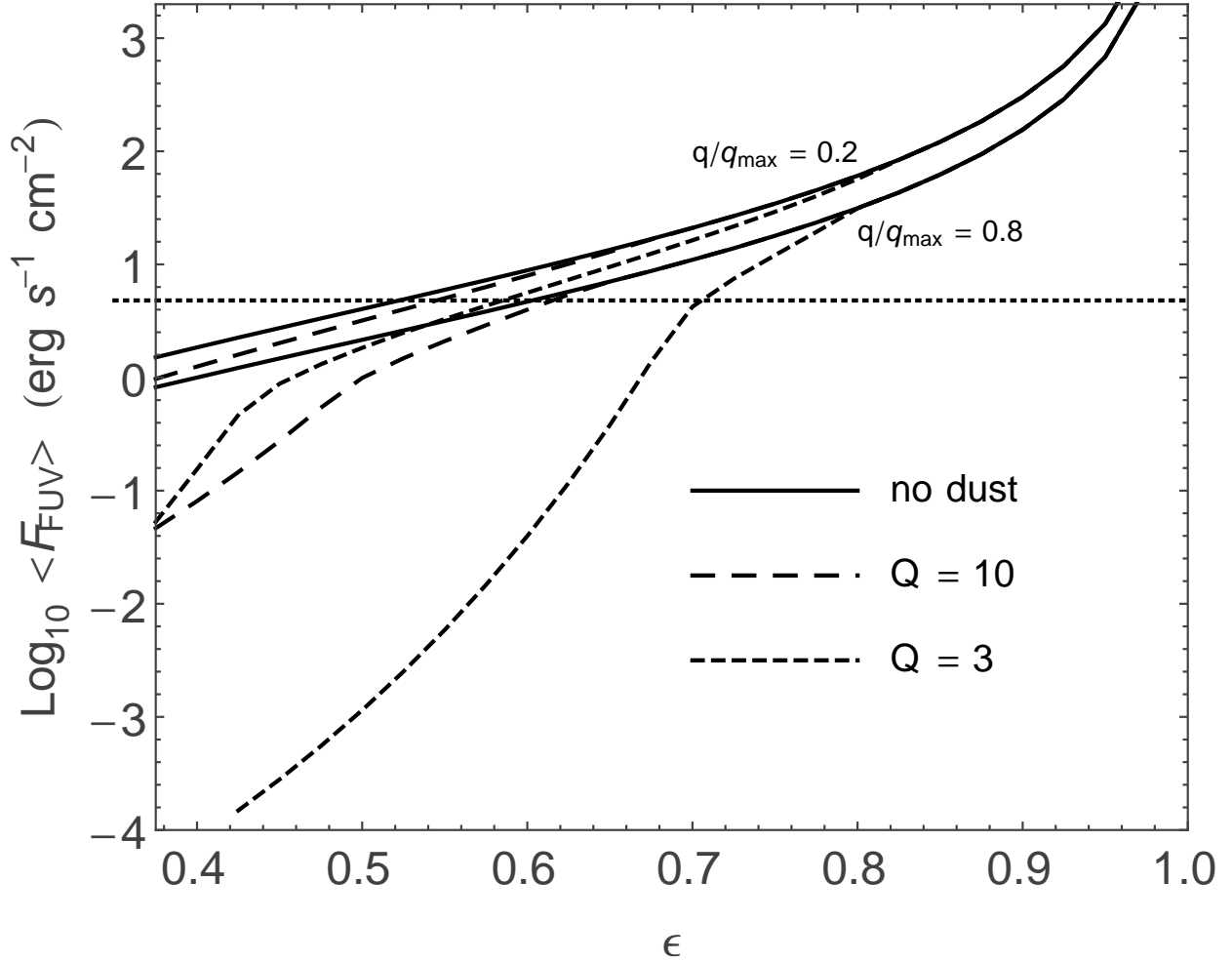


Fig. 7.— Orbit-averaged flux as a function of dimensionless energy  $\epsilon$  for  $q/q_{max} = 0.2$  (upper branch) and  $q/q_{max} = 0.8$  (lower branch) and three dust-extinction scenarios: no dust (solid curve);  $Q = 10$  (long-dashed curve); and  $Q = 3$  (short-dashed curve). For each case, clusters have Hernquist density profiles ( $c = 3$ ), star formation efficiencies  $\eta = 1/3$ , and  $N = 300$  stellar members. The dotted line represents the benchmark value as described in the text.

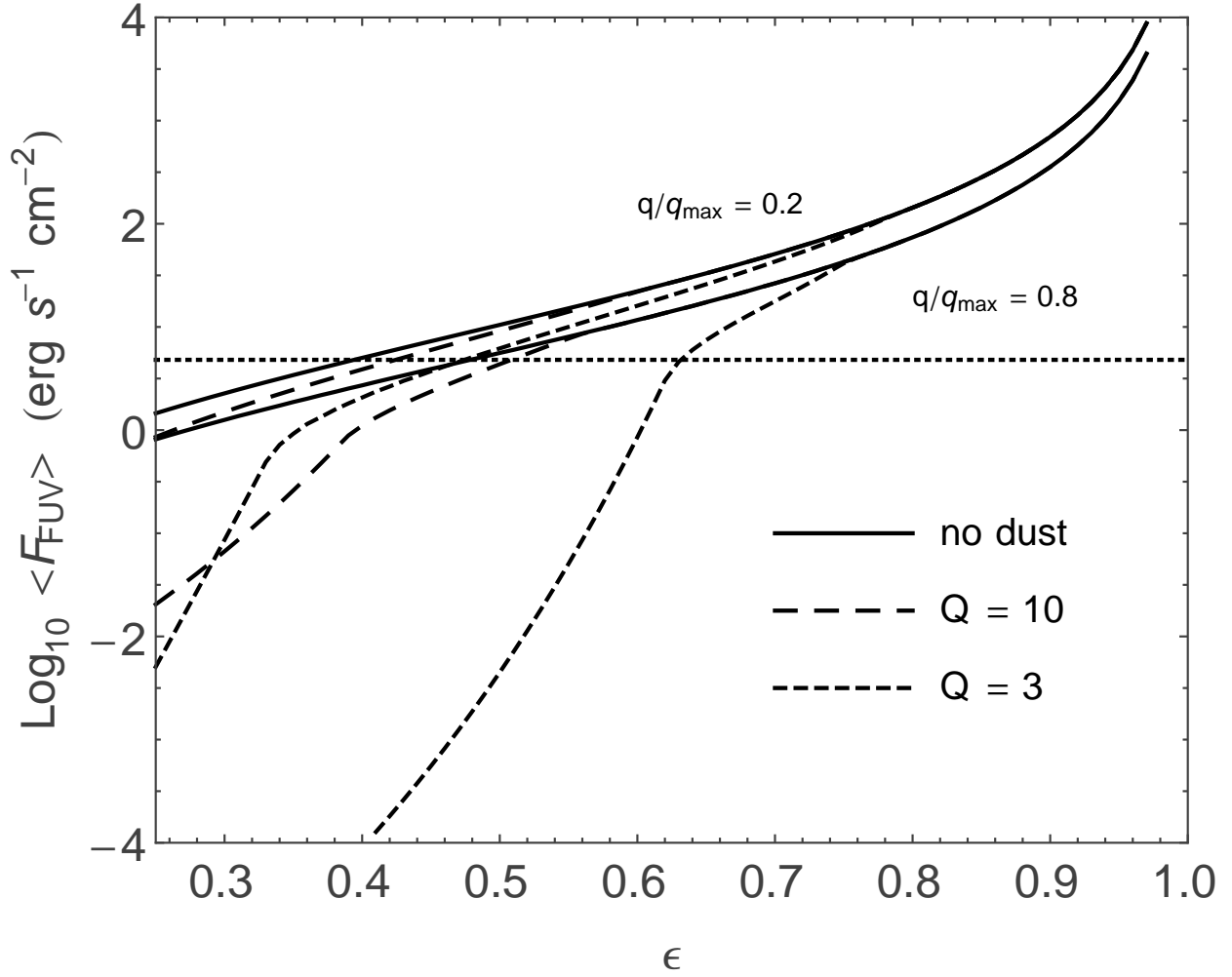


Fig. 8.— Same as Figure 7, but for clusters with modified Hernquist density profiles ( $c = 4$ ).

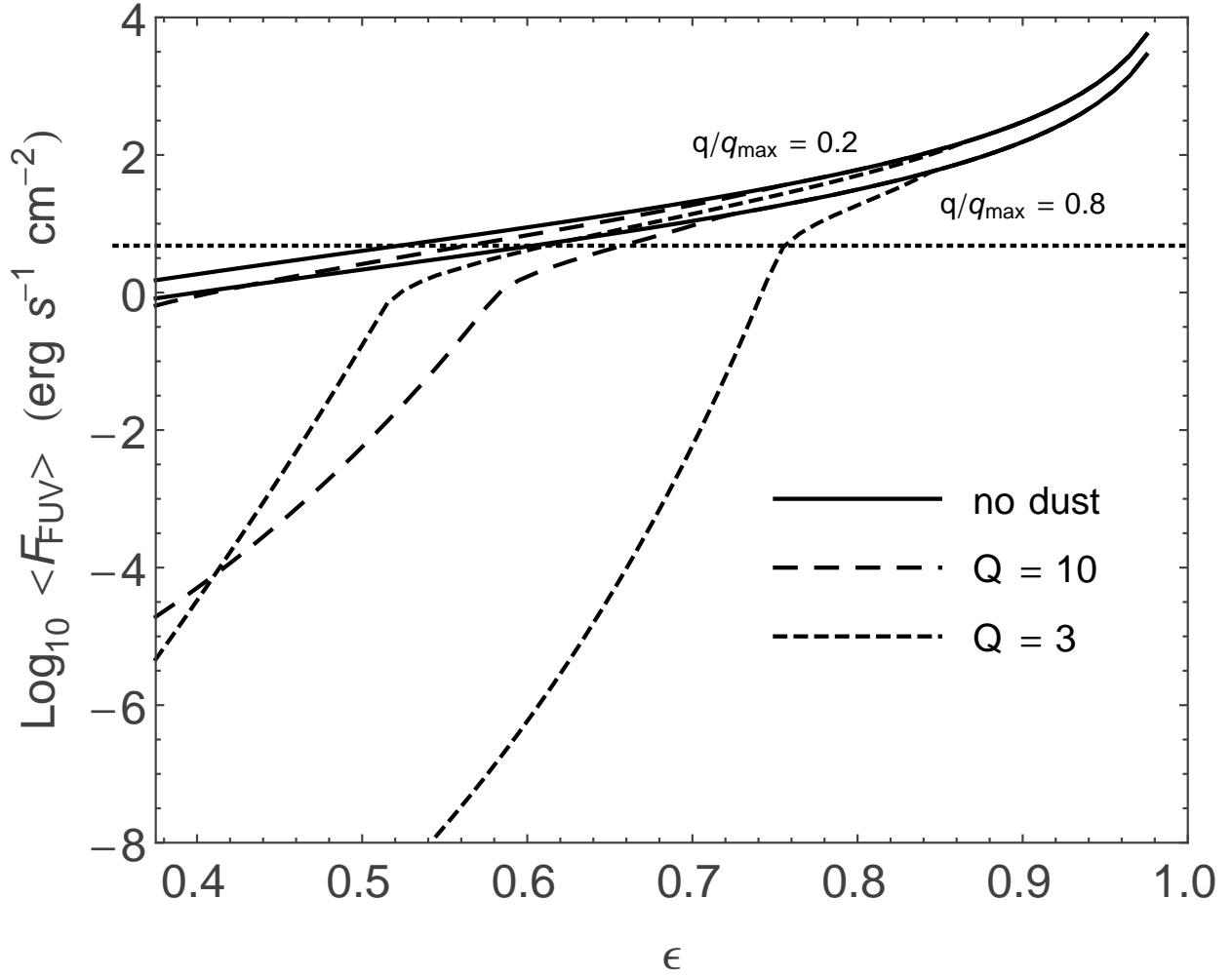


Fig. 9.— Same as Figure 7, but for clusters with star formation efficiencies  $\eta = 1/5$ .

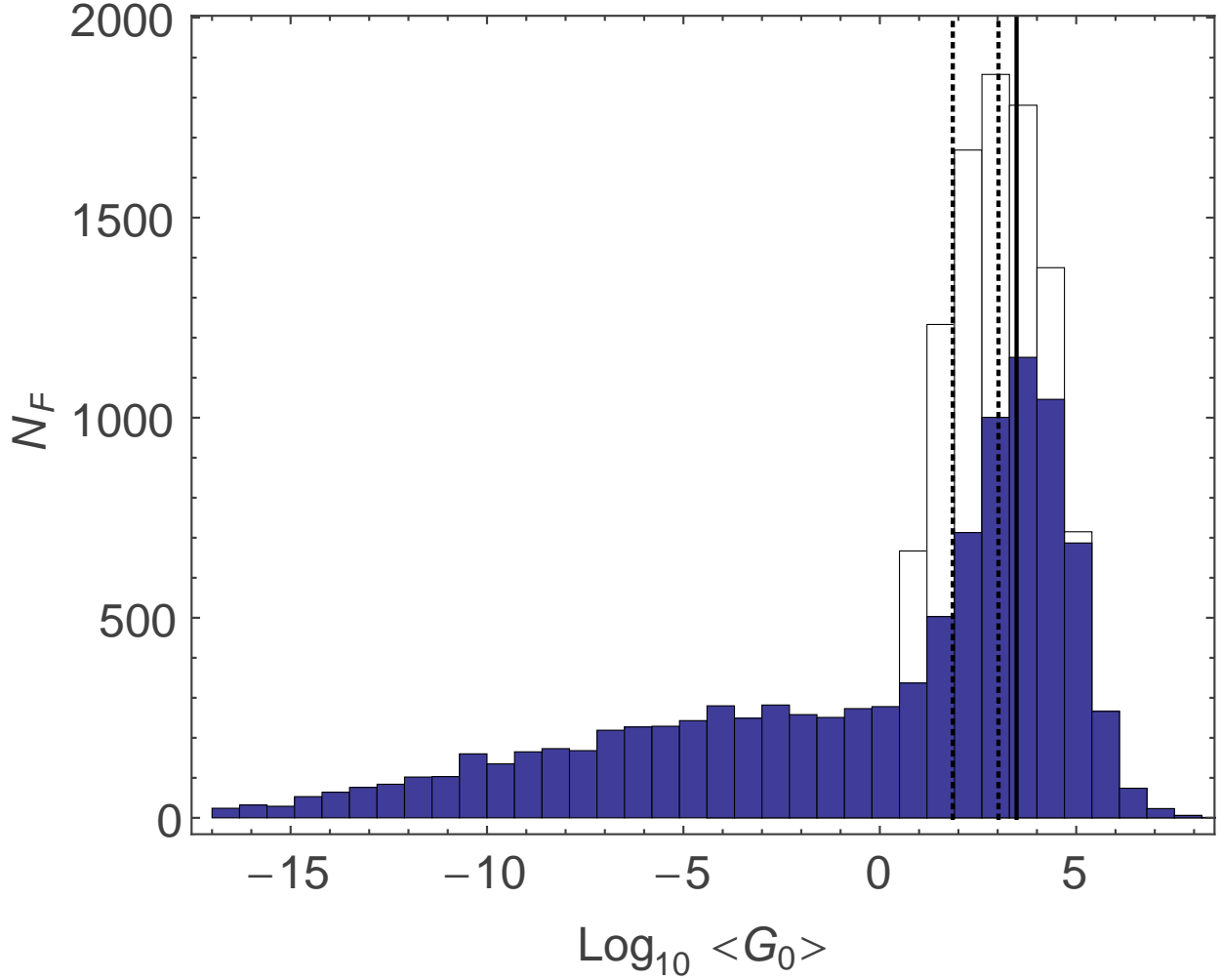


Fig. 10.— Orbit-averaged flux distributions for a sample of 10,000 stars with randomly selected orbital parameters  $\epsilon$  and  $q/q_{max}$  (as described in the text) for a cluster environment with  $N = 100$ ,  $c = 3$ , and  $\eta = 1/5$ . Flux values are expressed here in units of  $G_0$  (where  $G_0 = 1$  corresponds to a flux value of  $1.6 \times 10^{-3}$  ergs  $\text{s}^{-1}$   $\text{cm}^{-2}$ , which is close to the value of the interstellar FUV radiation field). The unshaded histogram represents the case with no dust. The shaded histogram represents the case with dust attenuation and  $Q = 3$ . The solid line represents our benchmark value, as described in the text. The dotted lines represent the median values of the two distributions, with the lower value corresponding to the case that includes dust attenuation.



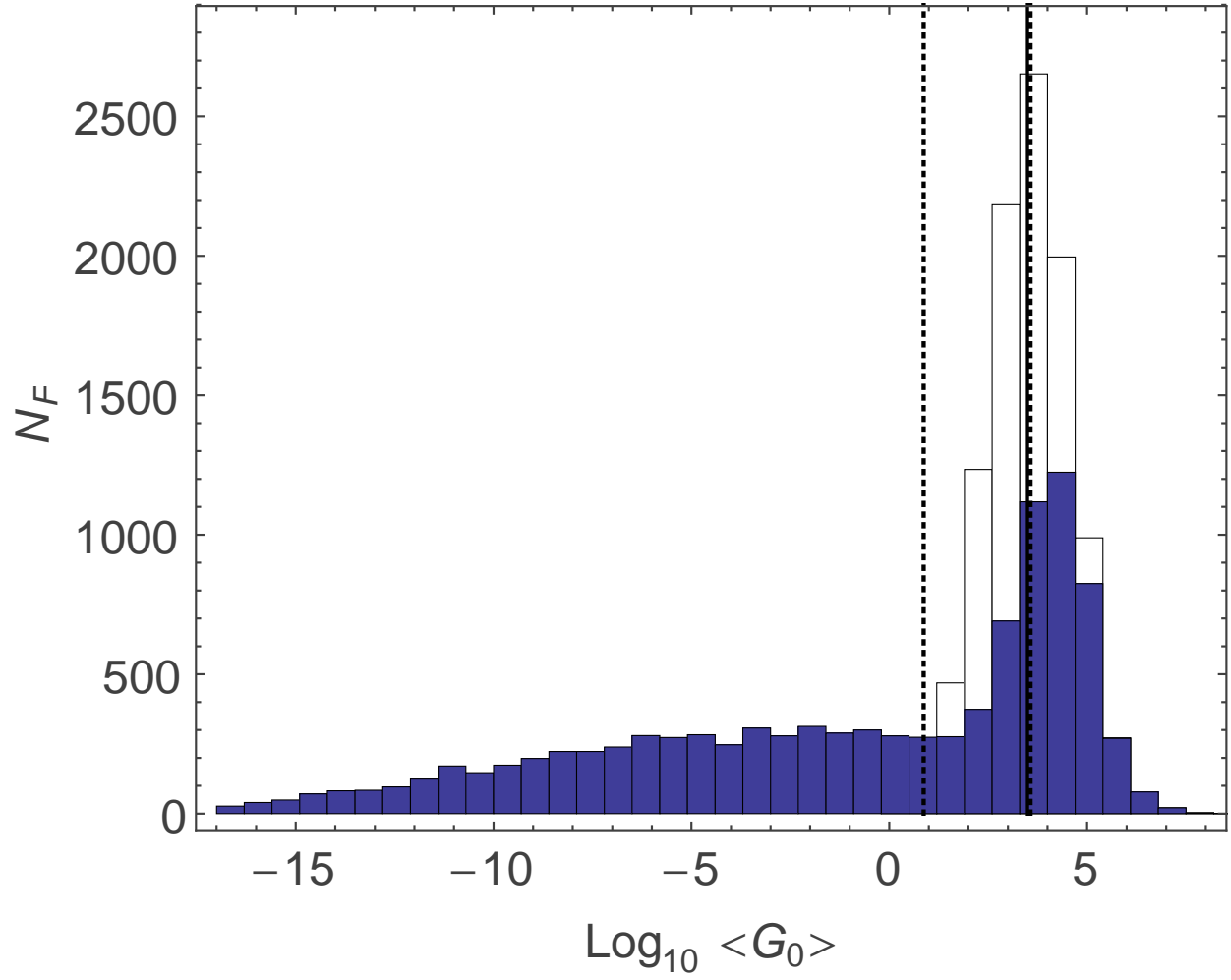


Fig. 11.— Same as Figure 10, but with stellar membership  $N = 300$ .

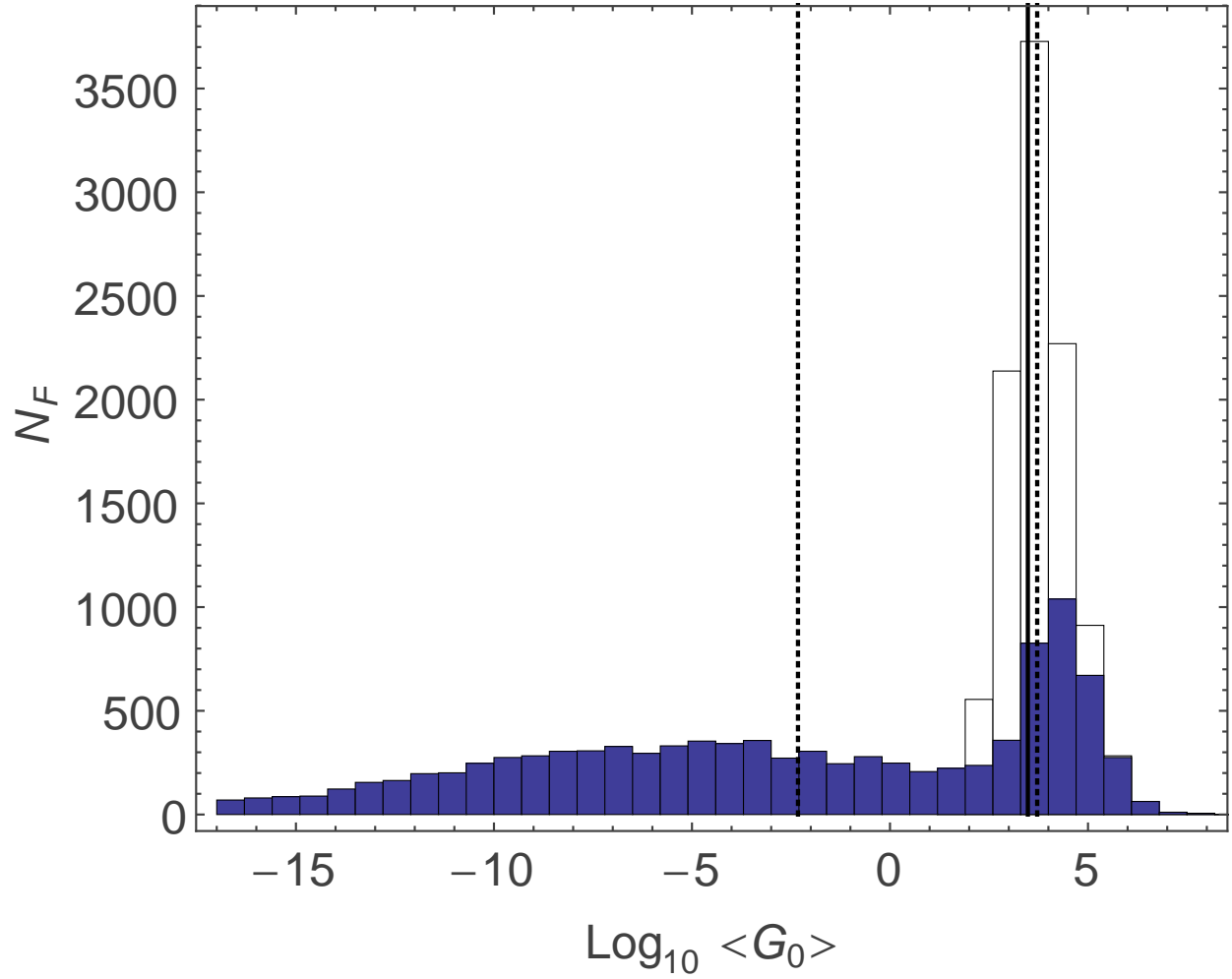


Fig. 12.— Same as Figure 10, but with stellar membership  $N = 1000$ .

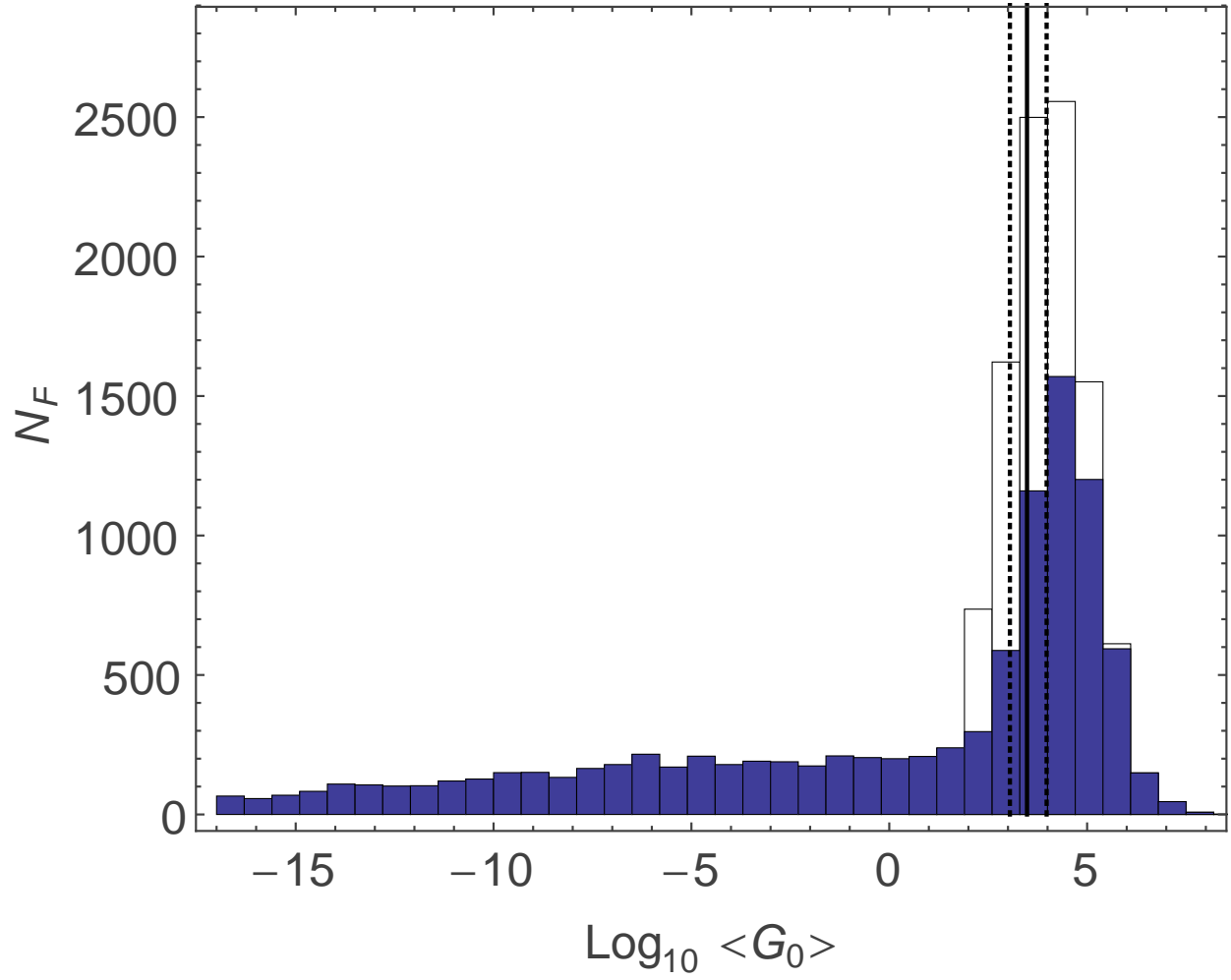


Fig. 13.— Same as Figure 11 ( $N = 300$ ,  $\eta = 1/5$ ,  $Q = 3$ ), but with density profile index  $c = 4$ .

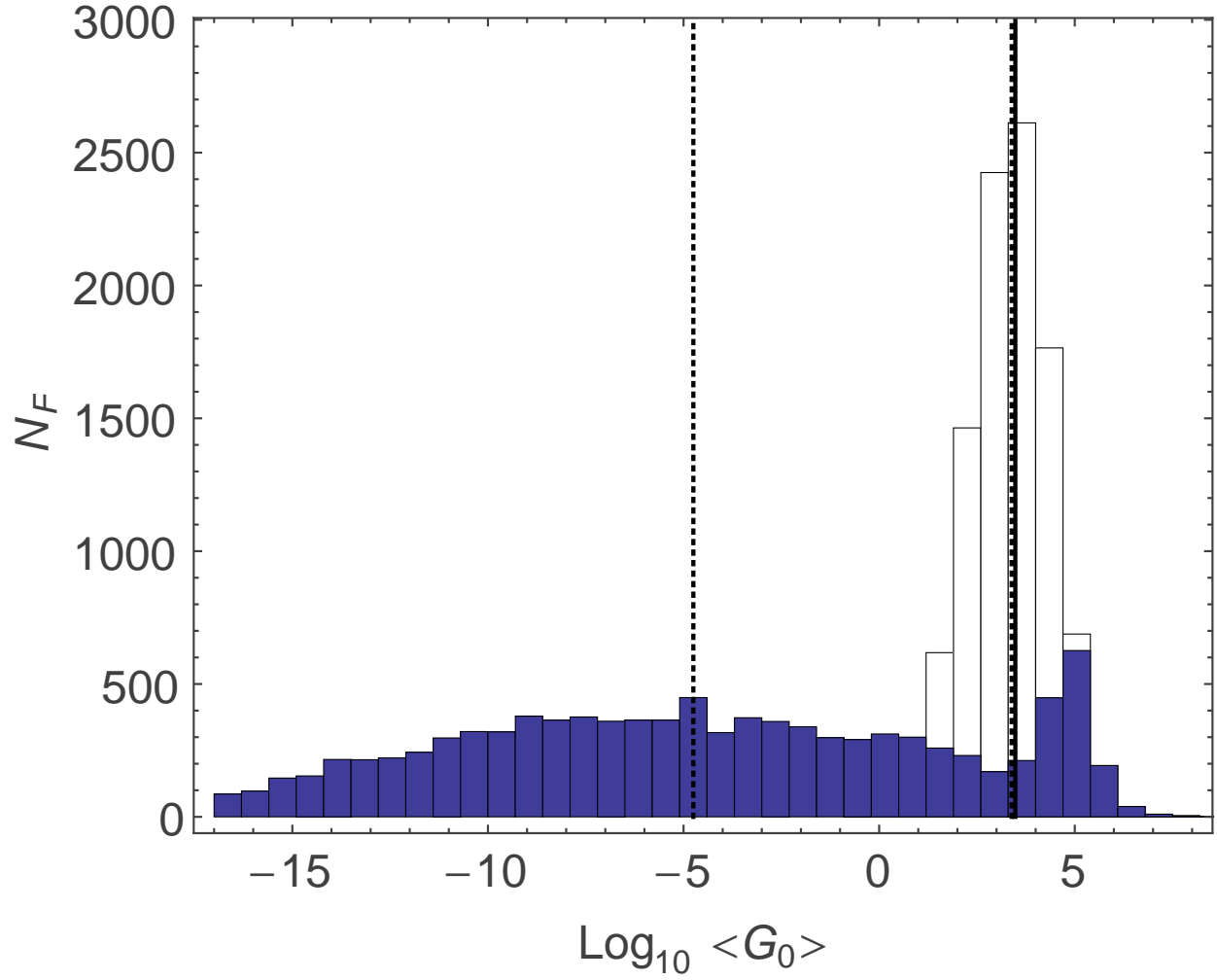


Fig. 14.— Same as Figure 11 ( $N = 300$ ,  $\eta = 1/5$ ,  $Q = 3$ ,  $c = 3$ ), but for circular orbits ( $q = q_{max}$ ).